Nanoscale

Defect Creation in WSe_2 with Microsecond Photoluminescence Lifetime by Focused Ion Beam Irradiation

Journal:	*Nanoscale*
Manuscript ID	NR-ART-09-2019-008390.R1
Article Type:	Paper
Date Submitted by the Author:	24-Nov-2019

Complete List of Authors:	Qian, Qingkai; Pennsylvania State University, Electrical Engineering Peng, Lintao; Argonne National Laboratory, Center for Nanoscale Materials Lopez, Nestor Perea ; Penn State University, Physics Fujisawa, Kazunori; The Pennsylvania State University, Department of Physics Zhang, Kunyan; Pennsylvania State University, Electrical Engineering Zhang, Xiaotian; Pennsylvania State University, Department of Materials Science and Engineering Choudhury, Tanushree ; The Pennsylvania State University, Materials Research Institute; The Pennsylvania State University Redwing, Joan; Penn State, Materials Science and Engineering Terrones, Mauricio; The Pennsylvania State University, Department of Physics; The Pennsylvania State University Ma, Xuedan; Argonne National Laboratory Huang, Shengxi; Pennsylvania State University, EE

ARTICLE

Defect Creation in WSe_2 with Microsecond Photoluminescence Lifetime by Focused Ion Beam Irradiation

Received 00th January 20xx,
Accepted 00th January 20xx

DOI: 10.1039/x0xx00000x

Qingkai Qian,[a] Lintao Peng,[b] Nestor Perea-Lopez,[c,d] Kazunori Fujisawa,[c,d] Kunyan Zhang,[a] Xiaotian Zhang,[e] Tanushree H. Choudhury,[f] Joan M. Redwing,[e, f] Mauricio Terrones,[c,d,e,f,g] Xuedan Ma[b] and Shengxi Huang*[a]

Defect engineering is important for tailoring the electronic and optical properties of two-dimensional materials, and the capability to generate defects of certain types at specific locations is meaningful for potential applications such as optoelectronics and quantum photonics. In this work, atomic defects are created in single-layer WSe_2 using focused ion beam (FIB) irradiation, with defect densities spanning many orders of magnitude. The influences of defects are systematically characterized. Raman spectroscopy can only discern defects in WSe_2 for FIB dose higher than 1×10^{13} cm^{-2}, which causes blue shifts of both A_1' and E' modes. Photoluminescence (PL) of WSe_2 is more sensitive to defects. At cryogenic temperature, the low-energy PL induced by defects can be revealed, which shows redshifts and broadenings with increased FIB doses. Similar Raman shifts and PL spectrum changes are observed for chemical vapor deposition (CVD) grown WSe_2 film. A four microsecond-long lifetime is observed in the PL dynamics, which is three orders of magnitude longer than the often observed delocalized exciton lifetime and becomes more dominant for WSe_2 with increasing FIB doses. The ultra-long lifetime of PL in single-layer WSe_2 is consistent with first-principle calculation results considering the creation of both chalcogen and metal vacancies by FIB, and can be valuable for photo-catalytic reactions, valleytronics and quantum light emissions owing to the longer carrier separation/manipulation time.

Introduction

Transition-metal dichalcogenides (TMDCs), such as MoS_2, $MoSe_2$, WS_2, and WSe_2,[1,2] have been extensively studied for both fundamental science and optoelectronic applications,[3-7] owing to their unique properties, including the atomic layer thickness, dangling-bond free surface, strong light absorption,[8,9] and layer-tuned direct/indirect bandgap.[10,11] Valley polarization of excitons can be realized in monolayer TMDCs by optical pumping, because of the broken inversion symmetry, strong spin-orbit coupling and the resulted locking of electronic spin and valley degrees of freedom.[12-14] However, valleytronics based on TMDCs typically relies on delocalized excitons, which have an intrinsically fast recombination lifetime due to the large exciton oscillator strength. This short lifetime has placed a strict limitation on the pseudo-spin manipulation before the valley depolarization.[15,16] Other than the delocalized excitons, recently it has been theoretically predicated and experimentally demonstrated that defect-bound excitons can also preserve the valley selectivity.[17,18] The selective creation of defect-bound excitons with long lifetime can lead to significant breakthroughs for the practical valleytronic applications.

Besides valleytronics, TMDCs are promising platforms for solid state quantum light emissions.[7,19-25] These semiconductors have great flexibility in heterogeneous assembly and are compatible with established optoelectronic processing technologies. Moreover, the atomically thin TMDCs have the advantage of efficient extraction of the emitted photons without suffering from internal reflections.[7,26] Single-photon sources based on TMDCs have already been demonstrated,[7,19-25] which can become crucial components for emerging technologies such as quantum communications, processing, and metrology. Even though the position of quantum emitters can now be deterministically controlled by nanoscale strain engineering,[22-25] this technique only locally modifies the bandgap and causes the funneling of excitons towards unknown defect traps within the electronic bandgap.[24,25] As a result, the uncontrolled impurity- or defect-induced bound excitons will

[a] Department of Electrical Engineering, The Pennsylvania State University, University Park, Pennsylvania 16802, United States. Email: sjh5899@psu.edu
[b] Center for Nanoscale Materials, Argonne National Laboratory, Argonne, Illinois 60439, United States
[c] Department of Physics, The Pennsylvania State University, University Park, Pennsylvania 16802, United States
[d] Center for 2-Dimensional and Layered Materials, The Pennsylvania State University, University Park, Pennsylvania 16802, United States
[e] Department of Materials Science and Engineering , The Pennsylvania State University, University Park, Pennsylvania 16802, United States
[f] 2D Crystal Consortium, The Pennsylvania State University, University Park, Pennsylvania 16802, United States
[g] Department of Chemistry, The Pennsylvania State University, University Park, Pennsylvania 16802, United States

† Electronic Supplementary Information (ESI) available: FIB parameters, DFT calculation of density of states, joint density of states and permittivity, fitting of PL dynamics with varied exponential components. See DOI: 10.1039/x0xx00000x

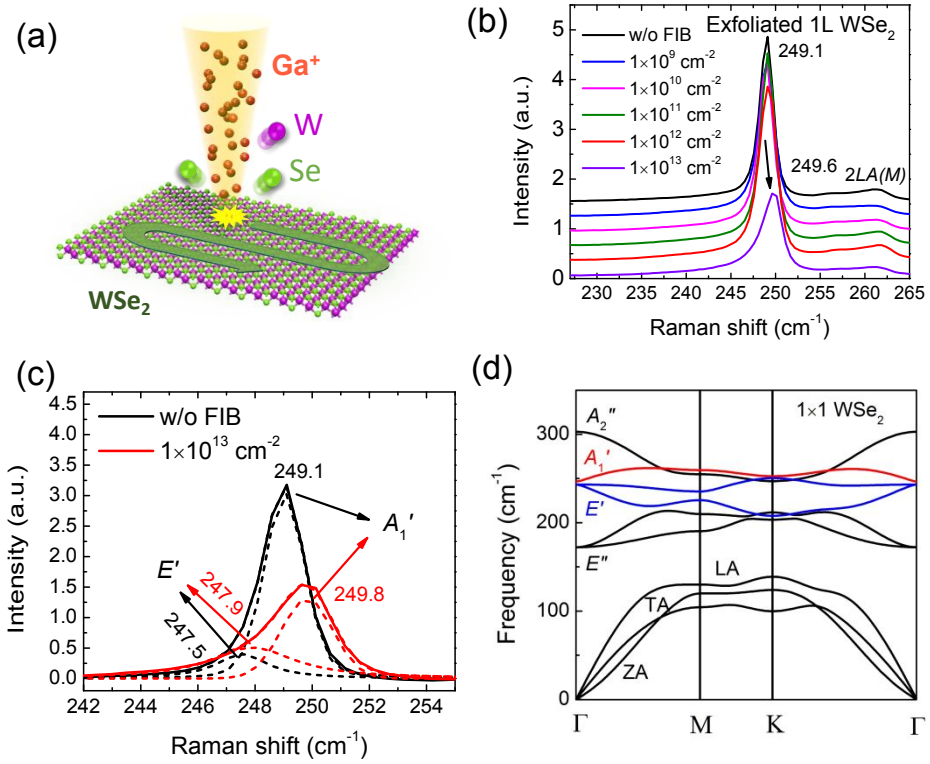

Fig. 1 (a) Schematic illustration of focused Ga^+ ion beam treatment of single-layer WSe_2. (b) Raman spectra of exfoliated single-layer WSe_2 before and after FIB treatment. Raman spectra are shifted vertically for clear view. FIB dose ranges from 1×10^9 to 1×10^{13} cm^{-2}. (c) Voigt fitting of Raman spectra and the peak assignments. FIB treatment causes a blue shift of A_1' and E' peaks. (d) Phonon dispersion of single-layer WSe_2. Phonon modes not at the Γ point are activated by the FIB defects and are responsible for the peak shifts.

emit photons with a broad energy distribution, which has brought a central obstacle to the development of single photon sources with high purity and indistinguishability based on TMDCs.

Controlled defect creation can be an important means to engineer the properties of TMDCs.[27-33] The lack of control over the presence and spatial distributions of defects in TMDCs will limit their utility for scalable devices. Addressing these challenges will facilitate the realization of devices with desirable electronic and optical properties for valleytronics and quantum technologies. In this work, focused ion beam (FIB) is used to introduce defects with controllable densities (ranging over 4 orders of magnitude) in WSe_2, which is the most widely reported 2D material for single-photon emitters among TMDCs.[7,19-25] Different from previous reported electron irradiation that mainly introduces chalcogen vacancy,[18,31] various types of defects including both chalcogen and metal vacancies or even nanopores can be created by FIB.[34] The influence of defects on the properties of WSe_2 are systematically examined by various characterization techniques, in conjunction with first-principles calculations. FIB irradiation introduces PL emission in single-layer WSe_2 with lower energy and longer lifetime, which becomes dominant in the PL dynamics for high FIB dose. At low temperature (10 K), lifetime as long as 4 μs is observed, which is almost three orders of magnitude longer than the often reported lifetime of delocalized excitons in the as-exfoliated WSe_2.[7,19] Because of the relatively simple processing steps and the nanometer spatial resolution of FIB, defect engineering via FIB can be a promising approach for modifying the optical properties of monolayer TMDCs.

Experimental section

Sample preparation. Single-layer WSe_2 is prepared by the tape-based mechanical exfoliation from the bulk WSe_2 crystal. The WSe_2 flakes are exfoliated on a Si substrate with 300-nm thermal oxidized SiO_2. Single-layer WSe_2 flakes are confirmed by color contrast under optical microscope and PL measurement. Almost-continuous WSe_2 films consisting of both single-layer and bilayer areas are prepared by a multistep gas-source CVD process on sapphire substrate. The substrate was inductively heated up to 800 °C under H_2 in a cold-wall vertical quartz tube reactor. $W(CO)_6$ and H_2Se were used as gas-phase precursors. The H_2Se flow rate was maintained at 7 sccm during the whole growth process, while multistep $W(CO)_6$ gas flow was introduced to the reactor to drive nucleation and promote lateral growth of WSe_2 domains. The detailed growth conditions and characterizations can be found in previous publication.[35]

FIB irradiation. The WSe_2 flakes are irradiated with focused Ga^+ ions using the ion gun of FEI Helios NanoLab 660 dual beam instrument. The acceleration voltage is fixed at 30 kV. The

incident ion beam is normal to the surface and followed a raster scan within a rectangular area of 410 μm long and 274 μm wide. The ion beam scans the sample in imaging mode, with a beam dwell time of 50 ns and a step size of 135 nm. The irradiation doses are controlled by the beam current and also the imaging frame number. To achieve four orders of magnitude of ion irradiation dose, the beam current intensity is tuned from 1.1 pA to 230 pA, while the scanning frame number is increased from 1 frame to 72 frames. The detailed FIB equipment settings and irradiaiton parameters can be found in the supplementary information (Table S1 and S2†).

Optical characterization. The Raman spectra and PL of WSe_2 at room temperature are measured by Horiba LabRam confocal microscope in the backscattering geometry. 532 nm laser is used, with a 100× objective. The laser spot has a diameter of about 1 μm. Notch filter of ±10 cm^{-1} and grating of 1800 g/mm are equipped. Low-temperature PL and PL dynamics is achieved by cooling the sample in a liquid helium cryostat to 10 K. 400 nm continuous-wave (CW) laser is used to excite WSe_2. The PL is recorded by Princeton Instruments SpectraPro HRS-750 together with a CCD (charge-coupled device) cooled by liquid nitrogen. PL dynamics are measured with a 31.2 kHz pulsed-laser excitation (400 nm) and counted by PicoQuant single-photon counting module. Band pass filters (680±50 nm and 820±50 nm) are used to selectively measure PL emission within a specific energy range.

Theoretical calculation. Phonon dispersions of single-layer WSe_2 are calculated by VASP and Phonopy codes. VASP is used to optimize the ground-state lattice structure and obtain the force constants. PBE functional and PAW potentials are adopted, with the van der Waals interaction corrected by the DFT-D3. Based on the force constants, phonon dispersion can be calculated by Phonopy codes. Supercells with vacuum layer of 18 Å are used to calculate the band structures of WSe_2 with Se and W vacancies. Plane-wave basis is set with cutoff energy of 400 eV. K-points with 7-by-7 Gamma-centered grids in reciprocal space are adopted. The vacancy contributions to defect levels are calculated by projection of the electronic states to the orbits of atoms adjacent to the vacancies.

Results and discussion

Mechanical exfoliation is used to prepare single-layer WSe_2. The single-layer WSe_2 flakes are identified by optical microscope and PL spectroscopy. Single-layer WSe_2 shows strong PL, while the PL of multilayer is significantly suppressed and has red-shifted peaks.[11,36] Focused Ga^+ ion beam (30 kV) is used to intentionally introduce atomic defects to WSe_2 with defect density controlled by the beam current and raster time. Similar FIB irradiation is recently utilized as a technique to isolate the bright emitters and to improve the single photon emission purity in exfoliated hexagonal boron nitride.[37] In principle, FIB has a great capability to achieve nanometer spatial resolution in creating defects,[38] however, the low defect density in WSe_2 also means that the PL signal from these defect levels would be submerged in the strong free exciton PL emissions. As an exploratory step, Ga^+ ion irradiation over the whole sample is conducted here to reveal the defect PL emission, with dose spanning four orders of magnitude from 1×10^9 cm^{-2} to 1×10^{13} cm^{-2}. Both chalcogen and metal vacancies of TMDCs can be introduced by the Ga^+ ion irradiations,[34] which is schematically illustrated in Fig. 1a. As a comparison, electron irradiation of WSe_2 has been reported and mainly creates chalcogen vacancies.[18,31] Moreover, FIB has much higher sputtering yield than electron irradiation: FIB dose of 1×10^{13} cm^{-2} could induce angstrom-size pores,[34,39] while electron irradiation of dose as high as 1×10^{14} cm^{-2} can only cause a barely visible change of the PL spectrum.[31] Based on the TEM statistics of high-dose FIB irradiation of MoS_2, it is found that each Ga^+ ion creates about 0.2 nanopores, and each nanopore consists of 2~8 vacancies.[34] It is reasonable to expect that similar defects can be created in WSe_2 by FIB. Because the FIB dose in this work is orders smaller, most of these defects will be single W or Se vacancies per site, instead of defect clusters. Only for high doses (e.g. 1×10^{13} cm^{-2}), complex vacancy clusters such as nanopores could be generated. Above all, it is reasonable to estimate that each Ga^+ ion creates approximately one vacancy in our experiment, and the FIB dose can be conveniently used to quantify the defect density.

The effect of Ga^+ ion irradiation on single-layer WSe_2 is first investigated by Raman spectroscopy using 532 nm excitation laser at room temperature. Because the in-plane and out-of-plane phonon modes (E' and A_1') of WSe_2 have very close frequencies, only one combined strong peak is observed. As shown in Fig. 1b, for ion doses smaller than 1×10^{13} cm^{-2}, no significant Raman spectra changes are observed. Only for the highest dose of 1×10^{13} cm^{-2}, the Raman scattering peak shifts and the intensity drops slightly. The Raman spectra before and after the ion irradiations are fitted with Voigt profiles, as shown in Fig. 1c. The intensities of both A_1' and E' peaks drop after ion irradiation. Moreover, the peaks show a blue shift after FIB treatment, especially for A_1' peak. These are caused by the activation of phonon modes at the Brillouin zone boundary.[40-43] As clearly shown in Fig. 1d, the branch of A_1' phonon has its minimum energy at the Γ point, and for pristine WSe_2, only phonon modes at the Γ point are active and observed during the first-order Raman scattering. Because of the Brillouin zone folding, the phonon modes not at the Γ point are activated by defects created by FIB and are responsible for the observed blue shift of Raman peaks.

PL of TMDCs can be more sensitive to defects.[31-34,44] Fig. 2a shows the PL spectra of single-layer WSe_2 before and after Ga^+ ion irradiations at room temperature, using 532 nm laser excitation. The PL spectra are normalized by the A_1' Raman peak, which provides a reasonable comparison of the PL intensity without the effects of laser focusing and substrate fluctuations (e.g. SiO_2 thickness), considering the Raman intensity is not very sensitive to defects. Defects created by FIB can act as trapping centers for excitons, which results in a rapid decrease of PL emission. No significant PL peak shifts are observed at room temperature, which is more clearly shown in Fig. 2b, where all PL spectra are normalized by the respective PL peak intensities, suggesting that most of the defect-trapped excitons recombine non-radiatively at room temperature. PL

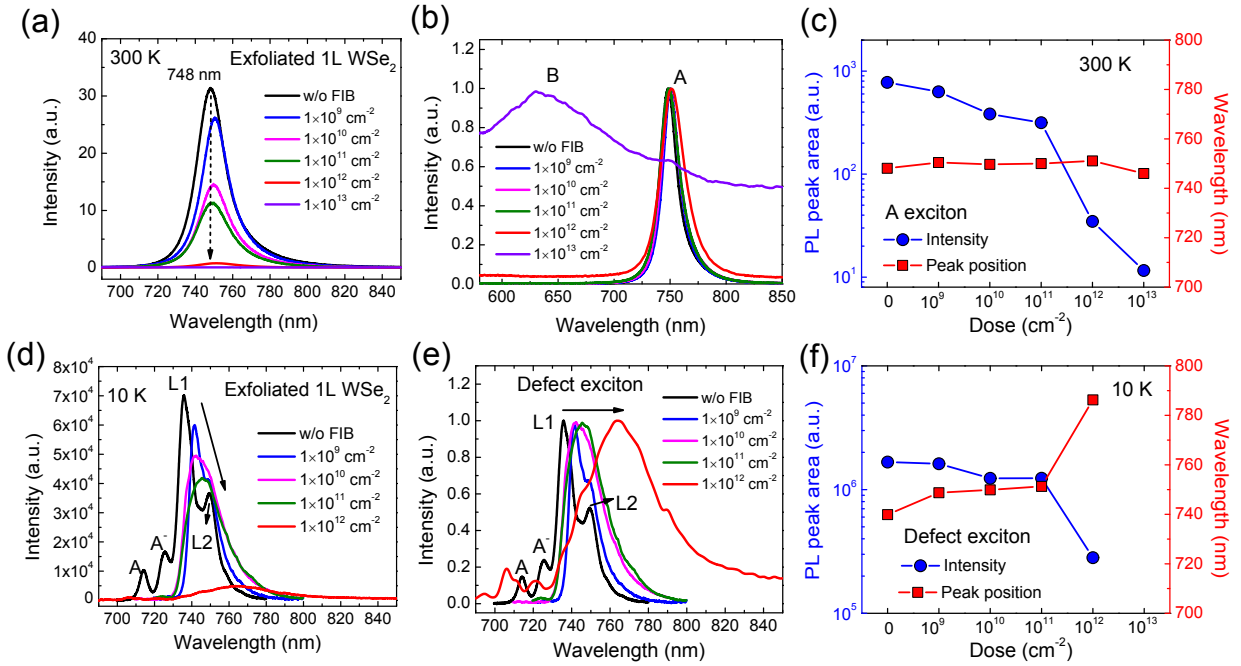

Fig. 2 (a) Photoluminescence (PL) spectra of exfoliated single-layer WSe_2 before and after FIB treatment at room temperature. (b) Peak-normalized PL spectra. (c) Integrated PL intensities and the PL peak positions of WSe_2 with different FIB doses. (d) PL spectra of exfoliated single-layer WSe_2 before and after FIB treatment measured at 10 K. (e) Peak-normalized PL spectra at 10 K. (f) Integrated PL intensities and the PL peak positions of WSe_2 with different FIB doses at 10 K.

peak width broadening only becomes obvious for doses larger than 1×10^{12} cm^{-2}. For the sample with the dose of 1×10^{13} cm^{-2}, the A exciton peak becomes so weak that B exciton appears to be stronger.[11] The peak areas (normalized by A_1' and E' Raman peaks) and peak shifts of A exciton are summarized in Fig. 2c.

The effect of Ga^+ ion irradiation on single-layer WSe_2 is further studied by low-temperature PL. 400 nm laser is used to excite WSe_2, with samples cooled to 10 K in a liquid helium cryostat. The measurement results are shown in Fig. 2d. For WSe_2 without FIB treatment, the peaks of both neutral (A^0) and charged (A^-) excitons can be clearly identified.[19,21,25] These exciton energies undergo a blue shift, compared with that at room temperature, which are caused by the thermal contraction of the WSe_2 lattice and the increased bandgap at low temperature.[11] Besides the delocalized neutral and charged excitons, the defect-bound excitons are also observed (labeled by L1 and L2 for pristine single-layer WSe_2),[45] in contrast to PL at room temperature. These defect-bound excitons can have stronger PL intensity than the delocalized excitons, even for single-layer WSe_2 without any FIB treatment, which is consistent with previous reports.[45] FIB treatment drastically changes the PL spectrum. First, PL from delocalized excitons becomes almost invisible. The PL intensity continuously drops and the peak position redshifts for single-layer WSe_2 with increased FIB doses. The PL intensity becomes so weak at 10 K for FIB dose of 1×10^{13} cm^{-2} that the PL intensity can hardly be measured. The peak shift trends can be more clearly seen by the peak-intensity-normalized PL spectra in Fig. 2e. Increasing FIB doses introduces PL emissions with smaller energy and also a wider energy distribution. Both the PL intensities and the PL peak positions at 10 K after FIB irradiations are summarized in Fig. 2f.

Controlled FIB treatments are also conducted for WSe_2 films prepared by chemical vapor deposition (CVD). CVD provides a scalable synthesis approach for TMDCs,[35,46,47] which is important for the practical applications of scalable devices and systems. Raman spectra of CVD WSe_2 before and after FIB treatment are shown in Fig. 3a. The Raman intensity is averaged for WSe_2 film in a 10 μm×10 μm area, realized by raster scanning of the laser beam, to avoid the fluctuations of CVD WSe_2 film thicknesses/qualities. Consistent with the result of exfoliated single-layer WSe_2 on SiO_2/Si substrate, the FIB treatment with dose of 1×10^{13} cm^{-2} causes the same Raman intensity drop and Stokes shift of Raman peaks. The PL spectra of CVD WSe_2 before and after FIB treatment at room temperature are plotted in Fig. 3b. Again, the PL spectra are normalized by their corresponding E' and A_1' Raman peaks. Compared with the PL of exfoliated single-layer WSe_2 (Fig. 2a), the PL spectra of CVD WSe_2 shows different features with ion irradiation. First, even without treatment, the PL intensity of CVD WSe_2 is almost 20 times weaker than the exfoliated one. Second, the observed PL peak has smaller energy: exfoliated sample has an emission wavelength of 748 nm, but CVD sample has a redshifted emission wavelength of 769 nm. Moreover, the PL intensities of CVD samples are insensitive to FIB treatment. The PL intensity of CVD WSe_2 only drops significantly for doses larger than 1×10^{12} cm^{-2}: PL intensity remains similar (within 4% change) for dose up to 1×10^{11} cm^{-2}, and drops to 80% and 33% of the original PL intensity only for doses of 1×10^{12} cm^{-2} and 1×10^{13} cm^{-2}, respectively. PL spectra of CVD WSe_2 at 10 K are

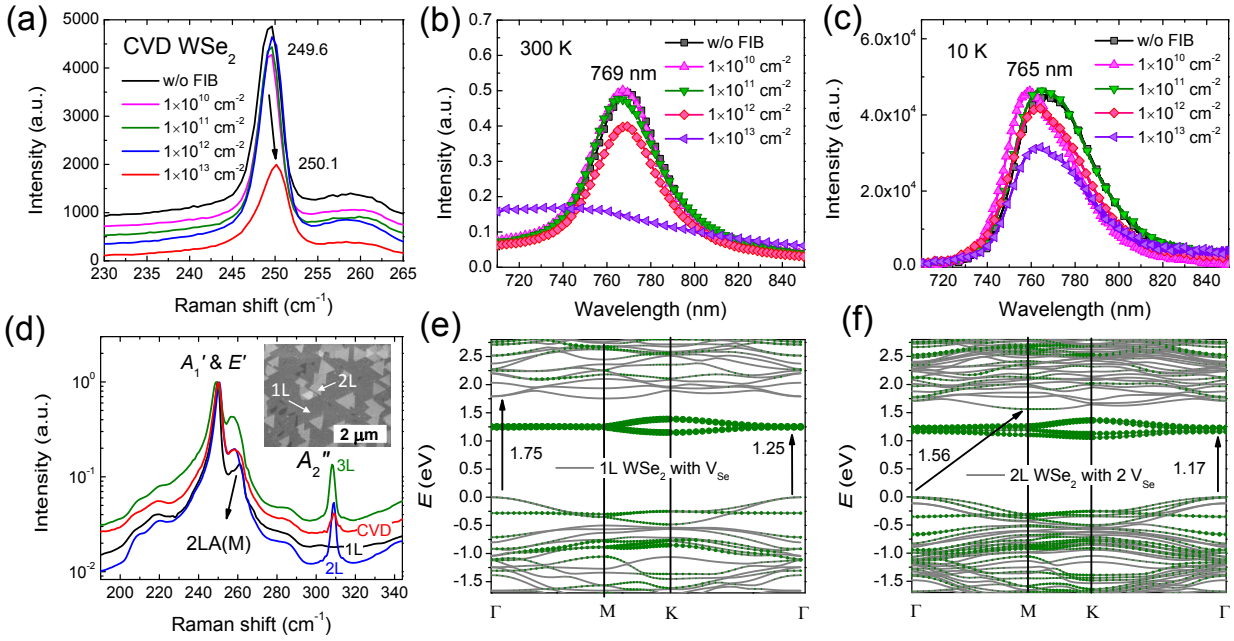

Fig. 3 (a) Raman spectra of CVD-grown WSe_2 before and after FIB treatment. Raman scattering intensity is averaged in a 10 μm×10 μm area. Raman spectra are shifted vertically for clear view. The same Stokes shift of Raman peak is observed for CVD WSe_2 with FIB dose of 1×10^{13} cm^{-2}. PL spectra of CVD WSe_2 before and after FIB treatment measured (b) at room temperature and (c) at 10 K. (d) Raman spectra of exfoliated multilayer WSe_2 and CVD WSe_2 plotted in logarithmic scale with a wider wavenumber range. Inset: SEM image of CVD-grown WSe_2. Bilayer WSe_2 flakes distribute on the continuous single-layer WSe_2 film as triangular islands. Electronic band structures of (e) single-layer WSe_2 and (f) bilayer WSe_2 with Se vacancies. The indirect-bandgap bilayer WSe_2 has made the conduction band closer to the defect levels.

plotted in Fig. 3c. Consistent with Fig. 3b, FIB treatment with low dose does not influence the PL spectra of CVD WSe_2 much, only the highest FIB dose (1×10^{13} cm^{-2}) causes the decrease of PL intensity by 32%.

The Raman spectrum of CVD WSe_2 with a wider wavenumber range including A_2" mode is plotted in Fig. 3d and compared with multilayer exfoliated WSe_2. The A_2" peak clearly suggests that multilayer WSe_2 exists in CVD grown WSe_2.[36,48] Since multilayer WSe_2 has different crystal symmetries and thus different notations of phonon modes, to maintain consistency, the same notations for single-layer WSe_2 are used here. Both the single-layer and bilayer WSe_2 flakes can be more clearly identified by the SEM image in the inset of Fig. 3d: bilayer WSe_2 islands (<0.7 μm) are located above the almost-continuous single-layer WSe_2,[35] and because of the small flake size, both single-layer and bilayer WSe_2 will be measured together during optical excitation. The PL intensities (peak areas) of CVD WSe_2 (Fig. 3b) and the exfoliated single-layer WSe_2 (Fig. 2a) become comparable for FIB dose of 1×10^{12} cm^{-2}. Because of the direct bandgap, single-layer WSe_2 usually has stronger PL intensity. If we assume that the PL in Fig. 3b is mainly contributed by single-layer CVD WSe_2, the above results suggest that the intrinsic defect density in CVD grown WSe_2 is on the order of 1×10^{12} cm^{-2}. However, as shown in Fig. 2b, even the highest dose (1×10^{13} cm^{-2}) treatment cannot change the A exciton PL peak position of exfoliated WSe_2 much at room temperature. Besides the growth defects, strain of single-layer WSe_2 after CVD growth on sapphire substrate could also contribute to the different PL peak positions and intensities. However, neither of them can totally explain the observed different PL peak positions/intensities of CVD WSe_2 and the insensitivity of PL intensities of CVD WSe_2 to FIB treatment.

The different PL spectra and defect response of CVD WSe_2 are most likely contributed by the bilayer islands of WSe_2. Bilayer WSe_2 has an indirect bandgap and its PL intensity is about one order weaker than single-layer WSe_2.[11,36] The PL peak of bilayer WSe_2 also coincides with the 769 nm peak observed for CVD WSe_2 at room temperature.[11,36] Bilayer WSe_2 present in the CVD samples can make the PL intensity of CVD WSe_2 more resistant to FIB irradiation. As widely known, bilayer has an indirect bandgap structure, and the excitons in bilayer WSe_2 can only recombine indirectly with the assistance of phonon scattering, which are distinct from that in single-layer WSe_2. The electronic band structures of single-layer and bilayer WSe_2 with the same Se vacancy densities are calculated in Fig. 3e and 3f. Relatively small supercell (3×3) is used here, because large supercell significantly increases the computational cost for bilayers. As can be clearly identified by Se vacancy contributions (the olive dot size), defect levels inside the bandgap are introduced by the Se vacancies[18]. These defect states will trap the delocalized excitons or electrons/holes and result in the PL emission with lower energy at low temperature.[17,18,49] The influence of vacancies can be further revealed by the calculated density of states, joint density of states and the permittivity in the supplementary information (Fig. S1, S2 and S3†). Both single-layer and bilayer WSe_2 show similar defect states, however, because the different direct/indirect bandgap type, the conduction band of bilayer WSe_2 is closer to the defect

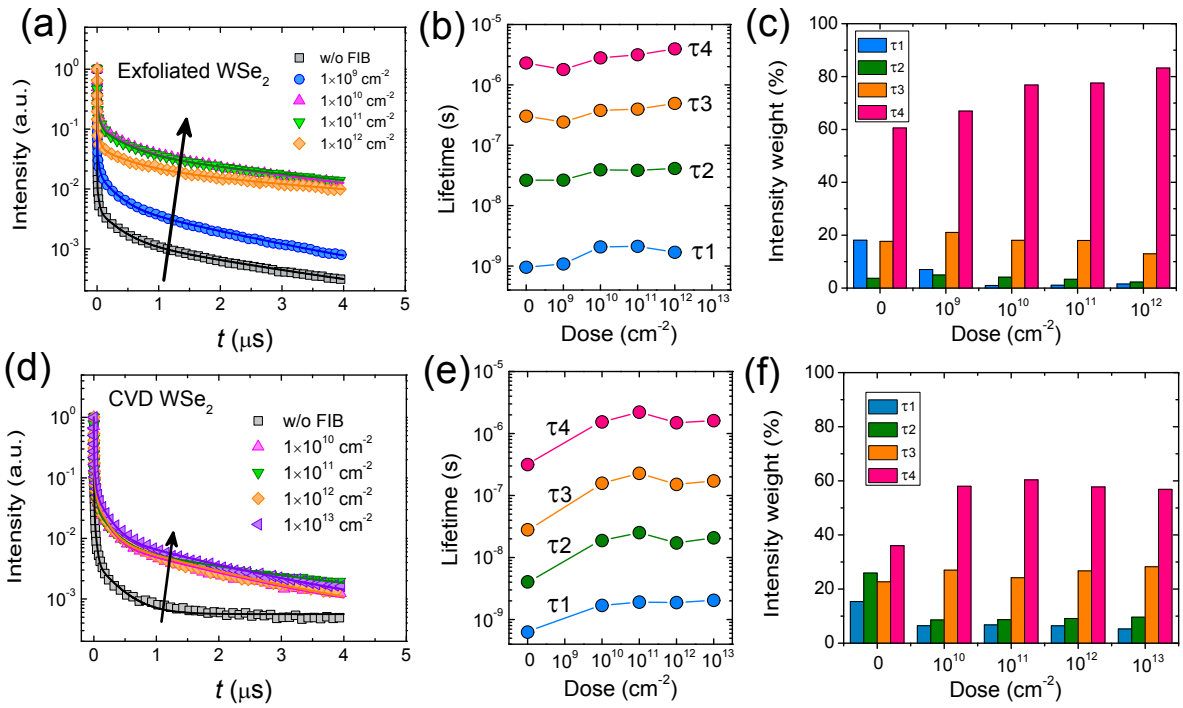

Fig. 4 (a) Time-resolved PL dynamics of exfoliated single-layer WSe_2 with different FIB doses, the solid lines are the fitting results using four exponential decays. (b) The extracted lifetimes of the four exponential components and (c) the corresponding intensity weights. (d) Time-resolved PL dynamics for CVD WSe_2 with different FIB doses, (e) the extracted lifetimes and (f) the corresponding intensity weights.

levels. The closer conduction band suggests that the defect-induced PL in bilayer WSe_2 will have smaller emission energy reduction than that of single-layer WSe_2. Moreover, from Fig. 2e it is found that the defect-bound excitons can even have emission energy larger than the PL peak of bilayer WSe_2 (Fig. 3c). All these results suggest that defect-induced PL emission are less energetically favorable in bilayer WSe_2 and it can explain why the PL of bilayer WSe_2 is less sensitive to FIB defects.

The effects of FIB treatment to WSe_2 are further studied by time-resolved PL dynamics, from which the exciton recombination processes can be revealed. 400-nm pulsed laser is used to excite WSe_2 at 10 K. PL dynamics are recorded using a single-photon avalanche diode. The measurement results for exfoliated single-layer WSe_2 with different FIB doses are shown by scatters in Fig. 4a. The PL signal follows a multi-exponential decay. For WSe_2 without FIB treatment, the PL intensity drops by 2 orders within 10 ns, consistent with the lifetime of previously reported localized excitons during single-photon emission in the as-exfoliated WSe_2.[7,19] FIB treatment clearly increases the average lifetime of PL, as indicated by the trend in Fig. 4a. As reported before, bound excitons associated with Se vacancies can have long lifetime (200 ns).[18] For PL dynamics within 300 ns, a biexponential decay fitting was needed.[18] In our experiment, the PL dynamics are measured for a much longer time range (4 μs), we find that at least four exponential decays are required to fit the PL dynamics. The necessity of four exponential decays are demonstrated by the fitting results for PL dynamics of WSe_2 without FIB, using varied exponential components (see supplementary information Fig. S4†). Limited exponential components can only fit the short time decays (Fig. S5†), because the least-square regression is conducted in linear scale. The fitting results for WSe_2 with varied FIB doses using four exponential components are plotted in Fig. 4a by the solid curves.

The lifetimes and intensity weights of the four exponential components are plotted in Fig. 4b and 4c. For all the samples, the PL dynamics includes four distinct lifetime components: ~1 ns, ~40 ns, ~500 ns and ~4 μs. The two fast components are consistent with the previously reported biexponential decay,[18] while the lifetime of slowest component is almost three orders longer than the often reported lifetime in the as exfoliated WSe_2, and is also much longer than that of the bright/dark excitons.[50] With increased FIB doses, the lifetime of each component does not change much. The major influence of FIB over PL is the different exponential component weights, as plotted by the histogram in Fig. 4c. Increasing FIB doses diminishes the short-lifetime excitons and increases the intensity weight of the long-lifetime component. For example, in the sample without FIB, the weight percentages of the four lifetime components are 18.1%, 3.7%, 17.7% and 60.5%, respectively, while these weights become 1.5%, 2.2%, 12.9% and 83.2% for sample with FIB does of 1×10^{12} cm^{-2}. The increased weights of long-lifetime components explain the observed slower decay of PL for WSe_2 with higher FIB doses. Recalling the PL peak redshifts of WSe_2 with higher FIB doses (Fig. 2e), the above results imply that FIB will cause more delocalized excitons to be trapped, and these defect-bound

excitons or the trapped electrons/holes in the defect levels tend to have longer lifetime. The sample with 1×10^{12} cm^{-2} dose shows a slightly faster decay of PL intensity than the samples of doses 1×10^{11} cm^{-2} and 1×10^{10} cm^{-2} in Fig. 4a, which could be caused by a slight sample variation due to the relatively weak PL intensity or the onset of defect cluster formation at high dose.[34] We note that the time-resolved PL dynamics are relatively more sensitive to short lifetime components, because the decay amplitude for each exponential component is proportional to the intensity weight but is inversely proportional to the lifetime. From the fitting results, 1×10^{12} cm^{-2} dose sample has relatively smaller lifetime τ_1 than doses 1×10^{11} cm^{-2} and 1×10^{10} cm^{-2}, while the intensity weight for τ_1 is larger, as a result, a sharper drop in PL dynamics is induced.

Similar PL dynamics and lifetime extractions are carried out for CVD WSe_2 before and after FIB treatment, the results are shown in Fig. 4d, 4e and 4f. Consistently, after FIB irradiation, the average lifetime of CVD WSe_2 increases. However, different from exfoliated single-layer WSe_2, the average lifetime of CVD samples does not increase further with FIB dose changing from 1×10^{10} cm^{-2} to 1×10^{13} cm^{-2} and is clearly shorter than that of exfoliated WSe_2. Considering the PL of CVD WSe_2 in Fig. 3c shows no significant changes after FIB irradiation, this non-sensitive lifetime of CVD WSe_2 can also be related to the bilayer WSe_2 in CVD samples: the smaller indirect bandgap has made the defect-bound or trapped excitons less energetically favourable and the indirect exciton emissions of bilayer WSe_2 are always important for the PL lifetime.

To further investigate the correlation between lifetime and PL emission energy, PL dynamics with different emission spectral ranges are measured. Band pass filters are used to select the PL emission, as noted by lower band pass filter (LBP, 680±50 nm) and higher band pass filter (HBP, 820±50 nm) in Fig. 5a. PL dynamics for the whole PL emission range without using any filters are noted by all pass (AP). The corresponding time-resolved PL dynamics are shown by the lower plot in Fig. 5a. For the same sample (exfoliated WSe_2 with 10^9 cm^{-2} FIB dose), excitons selected by LBP with larger exciton emission energies clearly have a shorter average lifetime, while the PL dynamics of all-pass (AP) excitons show an intermediate average lifetime. Using the same four-component exponential fitting, the lifetimes and corresponding intensity weights of these selected PL emissions are extracted and plotted in Fig. 5b and 5c. Even with a narrowed spectral range, these excitons still exhibit a broad distribution of lifetimes, which is consistent with previous report.[18] The high energy PL emissions (selected by LBP) tend to demonstrate significant short-lifetime components (~1 ns, ~10 ns), while the low-energy defect-bound or trapped excitons are almost contributed by a pure 4-μs long-lifetime component (87%). Recalling that the PL of WSe_2 with FIB dose of 1×10^{12} cm^{-2} shows a 83.2% contribution from the 4-μs long-lifetime component, this dominant long-lifetime component implies that limited defect species with low-energy PL emissions are controllably generated by FIB. With increasing FIB doses, more defect-bound excitons or trapped electrons/holes with smaller emission energy are generated, which have microsecond

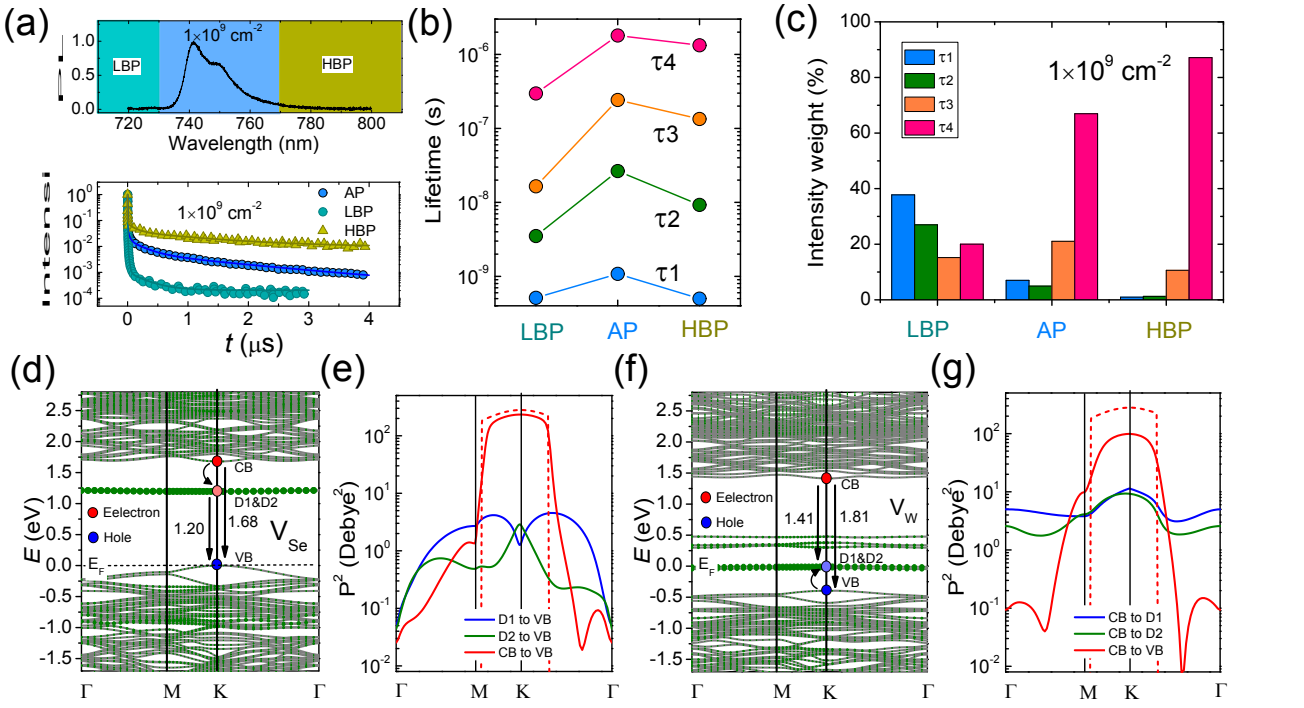

Fig. 5 (a) PL dynamics (lower plot) of excitons within different energy ranges for exfoliated single-layer WSe_2 with FIB dose of 10^9 cm^{-2}. The excitons are selected by low band pass (LBP), high band pass (HBP) and all pass (AP, i.e. no filter) filters as highlighted in the upper plot. (b) The specific extracted lifetimes and (c) the corresponding intensity weights of excitons within the selected energy ranges. (d) DFT calculated band structure of single-layer WSe_2 with one Se vacancy in a 5×5 supercell and (e) the corresponding transition dipole moments (squared and summed for x, y and z matrix components) between different bands. Dashed line indicates CB-VB transition on defect-free supercell. (f) Band structure with one W vacancy and (g) the corresponding transition dipole moments in 5×5 supercell.

lifetime and account for the measured long decay time of PL dynamics.

Both chalcogen and metal vacancies can be induced by FIB.[34] The PL lifetime associated with these defect-bound excitons or trapped electrons/holes can be theoretically studied with the assistance of DFT calculations.[51,52] To make the defect density more realistic and closer to the experimental conditions, a larger supercell (5×5) is adopted here for single-layer WSe_2, which has acceptable computational time for single-layer WSe_2. Other calculation results for varied supercell size can be found in the supplementary information (Fig. S6 and S7†). Even though defect clusters could be created in real irradiated samples,[34] given the relatively low dose and for simplicity here, only single Se and W vacancies are considered in the calculation. The band structure of 5×5 supercell with single Se vacancy is shown in Fig. 5d. Consistent with Fig. 3e, two defect levels are observed within the bandgap, but with smaller energy dispersion and splitting in k space, as indicated by the green dots of orbit projection weights. After optical excitation, electrons can be trapped to these unoccupied defect levels. Through recombination with holes in valance band, these trapped electrons can be responsible for the low-energy PL emission. More accurately, if the band dispersion and the Coulomb attraction between the electron and hole are considered, defect-bound exciton and its PL emissions can be studied.[51,52] The transition dipole moments (already squared and summed for x, y and z components of the transition dipole matrix) between different bands are calculated in Fig. 5e, which are related to spontaneous photon emission rates. Because of the small momentum of photon, only transitions between bands with the same k-point are considered. Since single-layer WSe_2 has a direct bandgap, the carriers will mostly recombine at K point. As can be clearly seen, transition from conduction band (CB) to valence band (VB) has much larger dipole moment than that from defect levels (D1 and D2) to VB. According to the Fermi's golden rule, the spontaneous emission rate is proportional to the squared sum of transition dipole moment via the following equation:[51,52]

$$\Gamma_{ck\to vk} = \frac{2\pi e^2}{\hbar}|\langle vk \,|\, \vec{r} \,|\, ck\rangle|^2 \frac{\hbar\omega}{2\varepsilon_0 V}\delta(E_{ck} - E_{vk} - \hbar\omega)$$

in which $|\langle vk \,|\, \vec{r} \,|\, ck\rangle|^2$ is the square summed transition dipole moment over x, y, z direction from band c to band v at k point, ω is the angular frequency of photon, ε_0 is vacuum permittivity, V is the volume of radiation field, and the δ-function denotes the conservation of energy. More accurately, transitions involving photon modes that satisfy the momentum and energy conservation should be summed to further account for the lifetime.[51,52] The large CB-VB dipole suggests that the high-energy PL emission from CB to VB has much shorter lifetime compared to emission from defect level to VB, which is consistent with the experimental results.

The transition dipole moment from CB to VB for ideal WSe_2 supercell with no defect is also calculated in Fig. 5e (red dashed line), which is even larger and should be more consistent with experimental conditions. Because of the Brillouin zone folding in supercell, some bands with different original k-points in unitcell are now folded to the same k-point of the supercell, causing the zero transition dipole moments at some k-points. Excitonic effects are not included in the above discussion, because the solving of Bethe–Salpeter equation for this large supercell is computationally expensive. However, since the excitonic state can be considered as a superposition state of electron-hole pairs, and the transition dipole of excitons can be calculated by a weight averaging of the transition dipole moments between bands,[51,52] the inclusion of excitonic effect should not change the lifetime trends much. As mentioned before, FIB can also cause metal defects.[34] Similar band structure and transition dipole moment calculations are conducted for single-layer WSe_2 with tungsten vacancy in Fig. 5f and 5g. Different from Se vacancy, W vacancy introduces five defect levels within the bandgap: two filled bands close to the valence band, and three empty bands close to the middle of the bandgap. The empty defect levels are too deep and only introduce PL emission energy much smaller than the experimental one, so they will not be considered here. The two filled defect levels can trap the holes and cause the observed low-energy PL emission through recombination with electrons from CB. The transition dipole moments between these bands are calculated in Fig. 5g. Similar to Se vacancy, the CB-VB transition also has much larger transition dipole moments than transitions involving the defect levels, suggesting that the W vacancy can also lead to long-lifetime low-energy PL emission.

Conclusions

The controllability over the presence, spatial distributions and density of defects offers an additional dimension to tune the material properties of TMDCs for optoelectronic applications. FIB irradiation with potential nanometer spatial resolution is well suited to controllably introduce defects inside the TMDC lattices and to facilitate the realization of devices with desirable optical and electronic properties. We have demonstrated that FIB irradiation is a promising approach for engineering defects in monolayer WSe_2. The influences of defects are systematically characterized by room-temperature Raman scattering/PL, low-temperature PL and PL dynamics. Raman spectroscopy can only discern the defects in WSe_2 with density higher than 1×10^{13} cm^{-2}, with blue shifts of both A_1' and E' peaks. At cryogenic temperature, exfoliated single-layer WSe_2 exhibits sensitive changes of PL intensities and emission energies with increased FIB doses, while comparatively the CVD WSe_2 is less sensitive because of the presence of bilayer flakes in our samples. FIB irradiation creates trapped electrons/holes or defect-bound excitons in single-layer WSe_2, which exhibit recombination lifetime as long as 4 μs. The intensity weights of this long-lifetime components increases and becomes almost dominant with high dose of ion beam irradiation. Under FIB irradiation, both chalcogen and metal vacancies can be created, and the related defect levels and the PL emission rates are studied with the assistance of DFT calculation, which show consistent lifetime trends with the experimental results. The physics behind this ultra-long lifetime, with the inclusion of both spin-orbit coupling and the excitonic effect, is worth further investigation. This FIB-created long lifetime of trapped

electron/hole or defect-bound exciton suggests potentially longer time for charge transfer/separation or quantum pseudo-spin manipulation, which can be useful in applications such as photo-catalytic reaction, quantum optical emission and valleytronics.

Conflicts of interest

There are no conflicts to declare.

Acknowledgements

The authors acknowledge the financial support through the Penn State 2D Crystal Consortium − Materials Innovation Platform (2DCC-MIP) under NSF cooperative agreement DMR-1539916. Use of the Center for Nanoscale Materials, an Office of Science user facility, was supported by the U.S. Department of Energy, Office of Science, Office of Basic Energy Sciences, under Contract No. DE-AC02-06CH11357.

References

1 Q. H. Wang, K. Kalantar-Zadeh, A. Kis, J. N. Coleman and M. S. Strano, *Nat. Nanotechnol.*, 2012, **7**, 699-712.
2 K. F. Mak and J. Shan, *Nat. Photonics*, 2016, **10**, 216-226.
3 A. Chernikov, T. C. Berkelbach, H. M. Hill, A. Rigosi, Y. Li, O. B. Aslan, D. R. Reichman, M. S. Hybertsen and T. F. Heinz, *Phys. Rev. Lett.*, 2014, **113**, 76802.
4 D. Qiu, F. da Jornada and S. Louie, *Phys. Rev. B*, 2016, **93**, 235435.
5 L. Yu, A. Zubair, E. J. G. Santos, X. Zhang, Y. Lin, Y. Zhang and T. Palacios, *Nano Lett.*, 2015, **15**, 4928-4934.
6 W. Zhang, J. Huang, C. Chen, Y. Chang, Y. Cheng and L. Li, *Adv. Mater.*, 2013, **25**, 3456-3461.
7 Y. He, G. Clark, J. R. Schaibley, Y. He, M. Chen, Y. Wei, X. Ding, Q. Zhang, W. Yao, X. Xu, C. Lu and J. Pan, *Nat. Nanotechnol.*, 2015, **10**, 497-502.
8 M. Bernardi, M. Palummo and J. C. Grossman, *Nano Lett.*, 2013, **13**, 3664-3670.
9 Y. Li, A. Chernikov, X. Zhang, A. Rigosi, H. M. Hill, A. M. van der Zande, D. A. Chenet, E. Shih, J. Hone and T. F. Heinz, *Phys. Rev. B*, 2016, **90**, 205422.
10 K. F. Mak, C. Lee, J. Hone, J. Shan and T. F. Heinz, *Phys. Rev. Lett.*, 2010, **105**, 136805.
11 A. Arora, M. Koperski, K. Nogajewski, J. Marcus, C. Faugeras and M. Potemski, *Nanoscale*, 2015, **7**, 10421-10429.
12 K. F. Mak, K. He, J. Shan and T. F. Heinz, *Nat. Nanotechnol.*, 2012, **7**, 494-498.
13 D. Xiao, G. B. Liu, W. Feng, X. Xu and W. Yao, *Phys. Rev. Lett.*, 2012, **108**, 196802.
14 H. Zeng, J. Dai, W. Yao, D. Xiao and X. Cui, *Nat. Nanotechnol.*, 2012, **7**, 490-493.
15 D. Lagarde, L. Bouet, X. Marie, C. R. Zhu, B. L. Liu, T. Amand, P. H. Tan and B. Urbaszek, *Phys. Rev. Lett.*, 2014, **112**, 47401.
16 K. Hao, G. Moody, F. Wu, C. K. Dass, L. Xu, C. Chen, L. Sun, M. Li, L. Li, A. H. MacDonald and X. Li, *Nat. Phys.*, 2016, **12**, 677-682.
17 S. Refaely-Abramson, D. Y. Qiu, S. G. Louie and J. B. Neaton, *Phys. Rev. Lett.*, 2018, **121**, 167402.
18 G. Moody, K. Tran, X. Lu, T. Autry, J. M. Fraser, R. P. Mirin, L. Yang, X. Li and K. L. Silverman, *Phys. Rev. Lett.*, 2018, **121**, 57403.
19 A. Srivastava, M. Sidler, A. V. Allain, D. S. Lembke, A. Kis and A. Imamoğlu, *Nat. Nanotechnol.*, 2015, **10**, 491-496.
20 M. Koperski, K. Nogajewski, A. Arora, V. Cherkez, P. Mallet, J. Y. Veuillen, J. Marcus, P. Kossacki and M. Potemski, *Nat. Nanotechnol.*, 2015, **10**, 503-506.
21 P. Tonndorf, R. Schmidt, R. Schneider, J. Kern, M. Buscema, G. A. Steele, A. Castellanos-Gomez, H. S. J. van der Zant, S. Michaelis De Vasconcellos and R. Bratschitsch, *Optica*, 2015, **2**, 347.
22 C. Palacios-Berraquero, D. M. Kara, A. R. P. Montblanch, M. Barbone, P. Latawiec, D. Yoon, A. K. Ott, M. Loncar, A. C. Ferrari and M. Atatüre, *Nat. Commun.*, 2017, **8**, 15093.
23 T. Cai, J. Kim, Z. Yang, S. Dutta, S. Aghaeimeibodi and E. Waks, *ACS Photonics*, 2018, **5**, 3466-3471.
24 S. Kumar, A. Kaczmarczyk and B. D. Gerardot, *Nano Lett.*, 2015, **15**, 7567-7573.
25 A. Branny, S. Kumar, R. Proux and B. D. Gerardot, *Nat. Commun.*, 2017, **8**, 15053.
26 P. Lodahl, S. Mahmoodian and S. Stobbe, *Rev. Mod. Phys.*, 2015, **87**, 347-400.
27 Z. Lin, B. R. Carvalho, E. Kahn, R. Lv, R. Rao, H. Terrones, M. A. Pimenta and M. Terrones, *2D Mater.*, 2016, **3**, 22002.
28 J. Hong, Z. Hu, M. Probert, K. Li, D. Lv, X. Yang, L. Gu, N. Mao, Q. Feng, L. Xie, J. Zhang, D. Wu, Z. Zhang, C. Jin, W. Ji, X. Zhang, J. Yuan and Z. Zhang, *Nat. Commun.*, 2015, **6**, 6293.
29 Z. He, R. Zhao, X. Chen, H. Chen, Y. Zhu, H. Su, S. Huang, J. Xue, J. Dai, S. Cheng, M. Liu, X. Wang and Y. Chen, *ACS Appl. Mater. Inter.*, 2018, **10**, 42524-42533.
30 Y. Chen, S. Huang, X. Ji, K. Adepalli, K. Yin, X. Ling, X. Wang, J. Xue, M. Dresselhaus, J. Kong and B. Yildiz, *ACS Nano*, 2018, **12**, 2569-2579.
31 Z. Wu, Z. Luo, Y. Shen, W. Zhao, W. Wang, H. Nan, X. Guo, L. Sun, X. Wang, Y. You and Z. Ni, *Nano Res.*, 2016, **9**, 3622-3631.
32 Z. Wu, W. Zhao, J. Jiang, T. Zheng, Y. You, J. Lu and Z. Ni, *J. Phys. Chem. C*, 2017, **121**, 12294-12299.
33 E. Mitterreiter, Y. Liang, M. Golibrzuch, D. McLaughlin, C. Csoklich, J. D. Bartl, A. Holleitner, U. Wurstbauer and A. S. Bandarenka, *npj 2D Mater. Appl.*, 2019, **3**, 1-9.
34 J. P. Thiruraman, K. Fujisawa, G. Danda, P. M. Das, T. Zhang, A. Bolotsky, N. Perea-López, A. Nicolaï, P. Senet, M. Terrones and M. Drndić, *Nano Lett.*, 2018, **18**, 1651-1659.
35 X. Zhang, T. H. Choudhury, M. Chubarov, Y. Xiang, B. Jariwala, F. Zhang, N. Alem, G. Wang, J. A. Robinson and J. M. Redwing, *Nano Lett.*, 2018, **18**, 1049-1056.
36 Q. Qian, Z. Zhang and K. J. Chen, *Phys. Rev. B*, 2018, **97**, 165409.
37 G. Grosso, H. Moon, B. Lienhard, S. Ali, D. K. Efetov, M. M. Furchi, P. Jarillo-Herrero, M. J. Ford, I. Aharonovich and D. Englund, *Nat. Commun.*, 2017, **8**, 705.
38 J. Klein, M. Lorke, M. Florian, F. Sigger, L. Sigl, S. Rey, J. Wierzbowski, J. Cerne, K. Müller, E. Mitterreiter, P. Zimmermann, T. Taniguchi, K. Watanabe, U. Wurstbauer, M. Kaniber, M. Knap, R. Schmidt, J. J. Finley and A. W. Holleitner, *Nat. Commun.*, 2019, **10**, 2755.
39 K. Yin, S. Huang, X. Chen, X. Wang, J. Kong, Y. Chen and J. Xue, *ACS Appl. Mater. Inter.*, 2018, **10**, 28909-28917.
40 S. Mignuzzi, A. J. Pollard, N. Bonini, B. Brennan, I. S. Gilmore, M. A. Pimenta, D. Richards and D. Roy, *Phys. Rev. B*, 2015, **91**, 195411.
41 W. Shi, M. Lin, Q. Tan, X. Qiao, J. Zhang and P. Tan, *2D Mater.*, 2016, **3**, 25016.
42 P. Maguire, D. S. Fox, Y. Zhou, Q. Wang, M. O'Brien, J. Jadwiszczak, C. P. Cullen, J. McManus, S. Bateman, N. McEvoy, G. S. Duesberg and H. Zhang, *Phys. Rev. B*, 2018, **98**, 134109.
43 J. Klein, A. Kuc, A. Nolinder, M. Altzschner, J. Wierzbowski, F. Sigger, F. Kreupl, J. J. Finley, U. Wurstbauer, A. W. Holleitner and M. Kaniber, *2D Mater.*, 2017, **5**, 11007.

44 S. Tongay, J. Suh, C. Ataca, W. Fan, A. Luce, J. S. Kang, J. Liu, C. Ko, R. Raghunathanan, J. Zhou, F. Ogletree, J. Li, J. C. Grossman and J. Wu, *Sci. Rep.*, 2013, **3**, 2657.
45 G. Wang, L. Bouet, D. Lagarde, M. Vidal, A. Balocchi, T. Amand, X. Marie and B. Urbaszek, *Phys. Rev. B*, 2014, **90**, 75413.
46 S. M. Eichfeld, L. Hossain, Y. Lin, A. F. Piasecki, B. Kupp, A. G. Birdwell, R. A. Burke, N. Lu, X. Peng, J. Li, A. Azcatl, S. McDonnell, R. M. Wallace, M. J. Kim, T. S. Mayer, J. M. Redwing and J. A. Robinson, *ACS Nano*, 2015, **9**, 2080-2087.
47 K. Kang, S. Xie, L. Huang, Y. Han, P. Y. Huang, K. F. Mak, C. Kim, D. Muller and J. Park, *Nature*, 2015, **520**, 656-660.
48 X. Zhang, X. Qiao, W. Shi, J. Wu, D. Jiang and P. Tan, *Chem. Soc. Rev.*, 2015, **44**, 2757-2785.
49 D. Wang, D. Han, D. West, N. Chen, S. Xie, W. Q. Tian, V. Meunier, S. Zhang and X. Li, *npj Comput. Mater.*, 2019, **5**, 1-6.
50 C. Robert, T. Amand, F. Cadiz, D. Lagarde, E. Courtade, M. Manca, T. Taniguchi, K. Watanabe, B. Urbaszek and X. Marie, *Phys. Rev. B*, 2017, **96**, 155423.
51 M. Palummo, M. Bernardi and J. C. Grossman, *Nano Lett.*, 2015, **15**, 2794-2800.
52 C. D. Spataru, S. Ismail-Beigi, R. B. Capaz and S. G. Louie, *Phys. Rev. Lett.*, 2005, **95**, 247402.

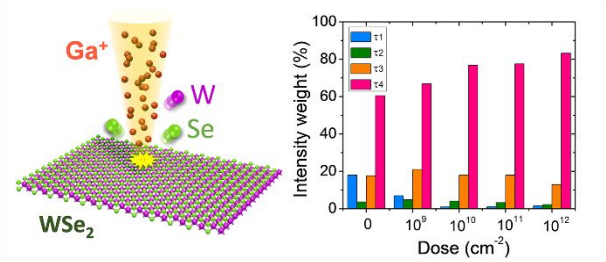

Atomic defects with a four microsecond-long photoluminescence lifetime are created in single-layer WSe_2 by focused ion beam irradiation.